Ionics (2021) 27:1049–1059
https://doi.org/10.1007/s11581-021-03901-9

ORIGINAL PAPER

Improved tin oxide nanosphere material via co-precipitation method as an anode for energy storage application in Li-ion batteries

S. Kumaraguru[1] · S. Raghu[2] · P. Rajkumar[3] · R. Subadevi[3] · M. Sivakumar[3] · Chang Woo Lee[4] · RM. Gnanamuthu[1]

Received: 30 July 2020 / Revised: 29 December 2020 / Accepted: 31 December 2020 / Published online: 8 January 2021

Abstract

The present proposed work, a design and fabrication of tin oxide nanosphere (SnO_2) using tin(II) oxyhydroxide and terephthalic acid composite materials, for the first time, via co-precipitation method. The morphology of the materials is found to be a well-crystalline nature and agglomerated with nanospherical shapes; it exhibits a 20–30-nm particle size. The electrochemical discharge–charge studies have been done using a half-cell (2032-sized coin type) at current rate 100 mA g^{-1} and within the potential range of 0.01 and 2.0 V vs. Li/Li^+. The impedance spectroscopy (EIS) and cyclic voltammetry (CV) studies are showing high resistance and a good oxidation–reduction properties. The cycle number vs. capacities illustrates the initial discharge capacity of 1149 mAh g^{-1} and the charge capacity retention from the second cycle (91%), respectively; it have been maintained up to the end of cycling. Thus, the prepared electrode can be developed for reversibility properties and possibly used as an anode for Li-ion batteries.

Keywords Secondary batteries · Efficiency · Nanospherical · Reversibility · Charge–discharge

Introduction

At present, ecologically clean energy-based research is consciously investigated by researchers to find an alternative to typical fossil fuel that has placed a huge threat in the earth's atmosphere [1, 2]. Lithium-ion batteries are the leading energy-producing devices for hybrid-electric vehicles and portable electronics like cell phones, laptops, and power tools [3, 4]. The establishment of new anode materials competent in furnishing high energy density and cycling stability as a substitute to conventional graphite anode remains to be daring in Li-ion battery research [5]. Several research works have been dedicated to diverse sorts of electrode materials with lost cost, cycle life, and high reversible capacity [6, 7]. Until now, various transition metal oxides such as CuO [8], Co_3O_4 [9], NiO [10], $NiMn_2O_4$ [11], and SnO_2 [12] and niobates such as $Al_{0.5}Nb_{24.5}O_{62}$ [13], $Zn_2Nb_{34}O_{87}$ [14], $V_3Nb_{17}O_{50}$ [15], and $Li_4Ti_5O_{12}$ [16] have scrutinized as a substitute electrode material for lithium-ion batteries.

Between these metal oxides, SnO_2 received much prodigious prominence in an extensive variety of technological applications such as Li-ion battery anode [17], gas sensing [18], photocatalyst [19], and solar cells [20]. It possesses low lithium alloying voltage and high theoretical capacity (782 mAh g^{-1}) compared with graphite (372 mAh g^{-1}) [21]. Nevertheless, the poor electrical conductivity and enormous volume change (300%) via conversion reaction during lithium insertion/extraction induce cracks, electrode pulverization, loss of active material, and unstable solid electrolyte

✉ RM. Gnanamuthu
gnanamur@srmist.edu.in; gnanamuthu.chem@gmail.com

[1] Batteries and Metal-Finishing Research Laboratory (+BMRL-), Department of Chemistry, SRM Institute of Science and Technology, SRM Nagar, Kattankulathur, Chengalpattu District, Tamil Nadu 603203, India

[2] Centre for Advanced Research and Development (CARD), Vels Institute of Science, Technology and Advanced Studies (VISTAS), Chennai, Tamil Nadu 600117, India

[3] #120, Energy Materials Lab, Department of Physics, Science Block, Alagappa University, Karaikudi, Tamil Nadu 630003, India

[4] Department of Chemical Engineering (Integrated Engineering) & Center for the SMART Energy Platform, College of Engineering, Kyung Hee University, 1732 Deogyeong-daero, Giheung, Yongin, Gyeongg 17104, South Korea

Fig. 1 Diagrammatic representation of the synthesis process for the SnO_2 nanoparticles

interphase (SEI films) which leads to the tremendous capacity fading [22–24]. To vanquish these issues, various approaches have been elaborated during the past years. There are two methodologies for making a composite electrode with conductive materials and prepare the nanomaterials with distinct morphologies [25]. All categories of SnO_2 nanostructures for instance nanotubes [26], nanowires [27], nanoboxes [28], nanosheets [29], nanorods [30], 3D flowers [31], hollow spheres [32], nanoparticles [33], and nanobelts [34] have successfully prepared to ameliorate the reversible capacity and long-lasting cycling life. In these, the nanoparticles comprise many benefits: (i) enhance the discharge capacity owing to its high surface area, which permits the high lithium-ion flux across the interface; (ii) active sites available for reversible reactions are high; and (iii) diminishing the lithium-ion diffusion pathways [35–37]. Faramarzi et al. reported that the SnO_2 particles synthesized via a vapor–solid process exhibit an initial capacity of 1818 mAh g^{-1} at 300 mA g^{-1}. The improved cycling performance attributed to the nanoribbon like morphology of the SnO_2 particles [38]. Zhao examined the Sb-doped SnO_2 nanospheres and conveyed that the prepared material conveys the first capacity of 1575 mAh g^{-1} to 6 at% of Sb dopant. The Sb dopants reduce the crystalline size and improve the electric conductivity, which leads to superior cycling performance [39]. Yin inspected the SnO_2 nanoparticles produced through the microwave hydrothermal method and found that the fabricated material displays a maximum capacity of 1196.63 mAh g^{-1} at 100 mA g^{-1}. The ultrafine nanostructural architecture of SnO_2 improves the kinetics of the electrochemical reaction between SnO_2 and Li-ion [40].

In general, when pure tin is used as a negative electrode in secondary batteries, the discharge and charge process between Sn and Li would induce huge volume change and internal stress, which leads to breakdown and poor electrical conductivity. Finally, it results in capacity declining upon prolonged cycling [41, 42]. There are lots of strategies that have been proposed using new composition and modification of the structure.

So, in this work, the synthesis of SnO_2 nanospheres from tin oxyhydroxide/terephthalic acid composite via co-precipitation method obtained the yield in gram quantities. There are several advantages of using terephthalic acid in the synthesis: (1) during calcination, it can be easily removed and form the product (SnO_2); (2) gives unique morphology and structure, (3) uniform-sized SnO_2 particles; and (4) it may lead to improved cycling performance. The synthesized SnO_2 nanoparticles are identified employing XRD, FT-IR, TGA, HR-SEM, and HRTEM, respectively. The electrochemical activities such as cyclic voltammetry, impedance, and discharge-charge are investigated to find out the interfacial structure assembly and real-time application characters.

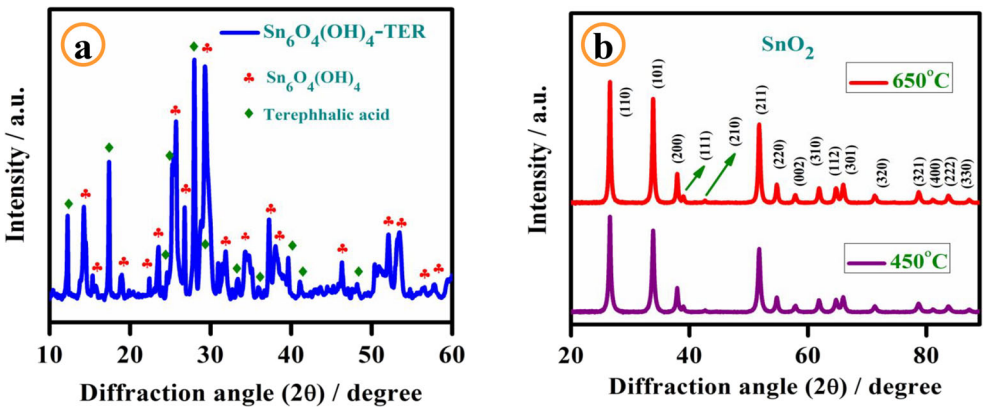

Fig. 2 **a** The XRD pattern of the tin oxyhydroxide-terephthalic acid composite. **b** The XRD patterns of SnO_2 nanoparticles calcined at 450 °C and 650 °C

Experimental section

Materials

$SnSO_4$ (≥ 95%, Sigma Aldrich), terephthalic acid (98%, Sigma Aldrich), NaOH (97%, Spectrum), ethanol (99.9%, Hayman), and Millipore water were utilized in the synthesis of tin oxyhydroxide/terephthalic acid composite.

Synthesis of tin oxyhydroxide/terephthalic acid composite ($Sn_6O_4(OH)_4$/TER)

In short, $SnSO_4$ (0.0669 M) was dissolved in 400 ml of H_2O under agitating. Terephthalic acid (0.0430 M) and NaOH (0.0860 M) were dissolved in 400 ml of water. With the constantly stirred solution, metal salts dissolved in water were mixed by dropwise addition and allowed to stir for 5 h. The colloidal white precipitate was filtered, sequentially washed with H_2O and EtOH. The residue was filtered and desiccated in an oven at 70 °C overnight. The synthesis process is sequentially illustrated in Fig. 1.

Synthesis of SnO_2 nanospheres

The $Sn_6O_4(OH)_4$/TERcomposite was pyrolyzed at 450 °C and 650 °C for 6 h under an air atmosphere at the ramp rate of 2 °C/min. The obtained product was naturally ventilated down to ambient temperature. Finally, the obtained product was ground well and stored for further physical as well as electrochemical studies.

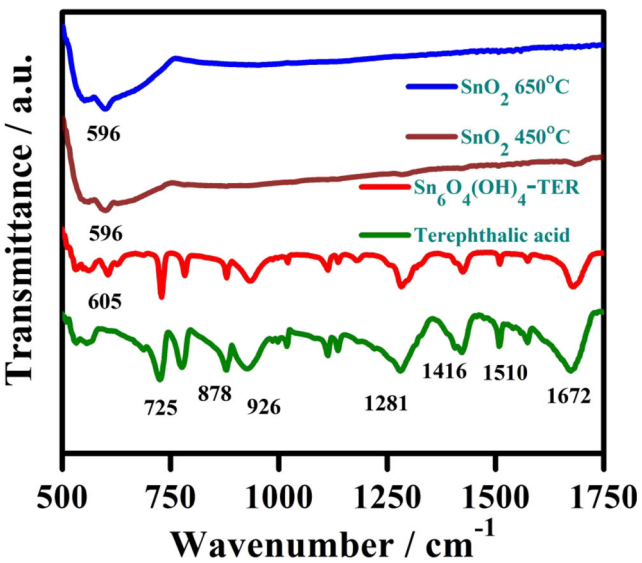

Fig. 3 The FT-IR spectra of the bare terephthalic acid, tin oxyhydroxide-terephthalic acid composite, and SnO_2 nanoparticles obtained at 450 °C and 650 °C

Instrumentation

The synthesized $Sn_6O_4(OH)_4$/TER composite and SnO_2 were confirmed with Bruker D8 Advance XRD furnished with copper Kα radiation (wavelength 1.5406 A) as an X-ray source and SSD160 LYNXEYE as a detector. The crystallite size value of synthesized SnO_2 reckoned using the Debye–Scherrer equation as follows [43]:

$$D = k\lambda/\beta\cos\theta$$

where k is the shape factor (0.9), λ is the wavelength of X-rays (0.15406 nm), β is the full width at half maximum, and θ is the angle of diffraction. The surface characterization of the prepared materials was studied with HRSEM (FEI Quanta FEG200) and a high-resolution transmission electron microscope (HR-TEM). The electronic state and surface chemical composition were examined with X-ray photoelectron spectroscopy (XPS) Thermo Scientific MULTILAB 2000 base system with X-ray, Auger, and ISS attachments. The N_2 gas adsorption–desorption isotherm was acquired on a Quantachrome NovaWin Instrument. Electrochemical experiments were performed with the Neware battery cycler. Thermal stability and vibrational frequency analyses of the synthesized materials were investigated with Netzsch-STA 2500 Regulus in a nitrogen atmosphere at a heating rate of 20 °C/min and SHIMADZU IR Tracer-100, respectively.

Coin cell assembling system

The metal oxide coating was equipped by the doctor blade method. The slurry has been prepared by mixing SnO_2 (70 wt%), Super-P carbon (20 wt%), PVDF (10 wt%), and an appropriate amount of NMP and cast over the copper foil. The coated foil was desiccated in an oven at 120 °C. The

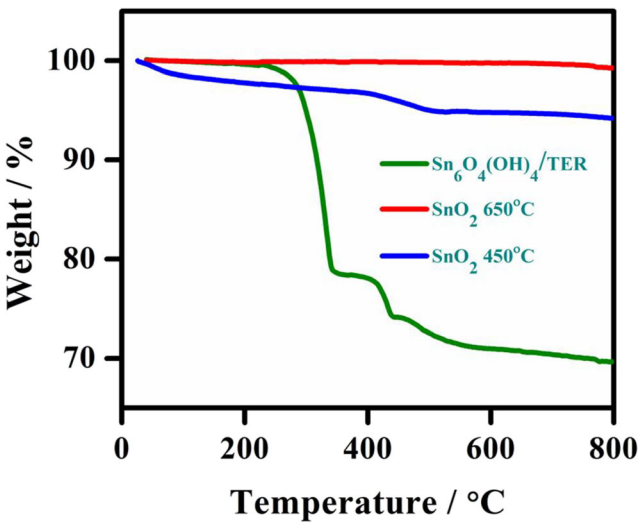

Fig. 4 The TGA plot of prepared tin oxyhydroxide-terephthalic acid composite and SnO_2 nanoparticles obtained at 450 °C and 650 °C

measured dry film thickness of the coating was about 110 μm. Li acts as both the counter and a reference electrode. Celgard 2531 and coated Cu foil were used as the separator and working electrodes, respectively. $LiPF_6$ (1 M) dissolved in 1:1 (v/v) ratio of EC/DMC mixture as electrolyte. The 2032 type coin cells were fabricated in an Ar-filled glove box. The electrochemical impedance (EIS) analysis was accomplished in the frequency range from 1 to 10 mHz with the amplitude perturbation of 10 mV. Galvanostatic discharge–charge investigations were performed at 100 mA g^{-1} and cutoff range between 0.01 and 2.0 V vs. Li/Li^+. The cyclic voltammetric experiment was executed in the potential window of 0.01 to 2.0 V vs. Li/Li^+ at the sweep rate of 0.1 mV s^{-1}.

Results and discussion

Physical characterization

Figure 2 illustrates the powder X-ray diffractograms of the $Sn_6O_4(OH)_4$/TER composite and SnO_2. Figure 2 a shows the highly crystalline nature of $Sn_6O_4(OH)_4$/TER composite, and the peaks indexed to the single-phase $Sn_6O_4(OH)_4$ (JCPDS card no. 46-1486) and terephthalic acid [44, 45]. Figure 2 b portrays the phase purity of SnO_2 and all the peaks marked to the SnO_2 (JCPDS card no. 88-0287) [46]. The SnO_2 particles expose peaks at 2 theta value of 26.57°, 33.88°, 37.96°, 38.98°, 42.65°, 51.79°, 54.71°, 57.87°, 61.86°, 64.73°, 65.99°, 71.34°, 78.66°, 81.09°, 83.71°, and 87.27° that correspond to the (110), (101), (200), (111), (210), (211), (220), (002), (310), (112), (301), (320), (321), (400), (222), and (330) crystal planes, respectively. The SnO_2 prepared at 450 °C and 650 °C portrays the crystallite size value of 18.91 and 26.33 nm. The SnO_2 prepared at 650 °C exhibits highly crystalline than the SnO_2 prepared at 450 °C.

Figure 3 displays the FT-IR spectra of the bare terephthalic acid, $Sn_6O_4(OH)_4$/TER composite, and SnO_2. The terephthalic acid and synthesized $Sn_6O_4(OH)_4$/TER composite divulges peaks at 1672 and 1510 cm^{-1} that were associated with asymmetric and symmetric stretching vibrations of the carbonyl group. The peaks noted at 1416, 1281, 926, 878, and 725 cm^{-1} were related to the C=C stretching, C–C stretching, O–H bending, C–H bending, and out-of-plane aromatic ring bending, respectively [47]. The synthesized $Sn_6O_4(OH)_4$/TER composite expresses vibrational frequencies similar to that of bare terephthalic acid. In addition to that, the stretching frequency appeared at 605 cm^{-1} indicates the formation of tin oxyhydroxide [48]. The stretching frequency observed at 596 cm^{-1} corresponds to the O–Sn–O bond formation. The broadness is a sign of tin oxide formation, and all other peaks of terephthalic acid have vanished for tin oxide prepared at 450 and 650 °C.

Figure 4 represents the thermogravimetric investigation of the $Sn_6O_4(OH)_4$/TER composite and SnO_2. The prepared $Sn_6O_4(OH)_4$/TER composite establishes a first weight loss in between the temperature of 242.5 °C and 345.5 °C (20.58

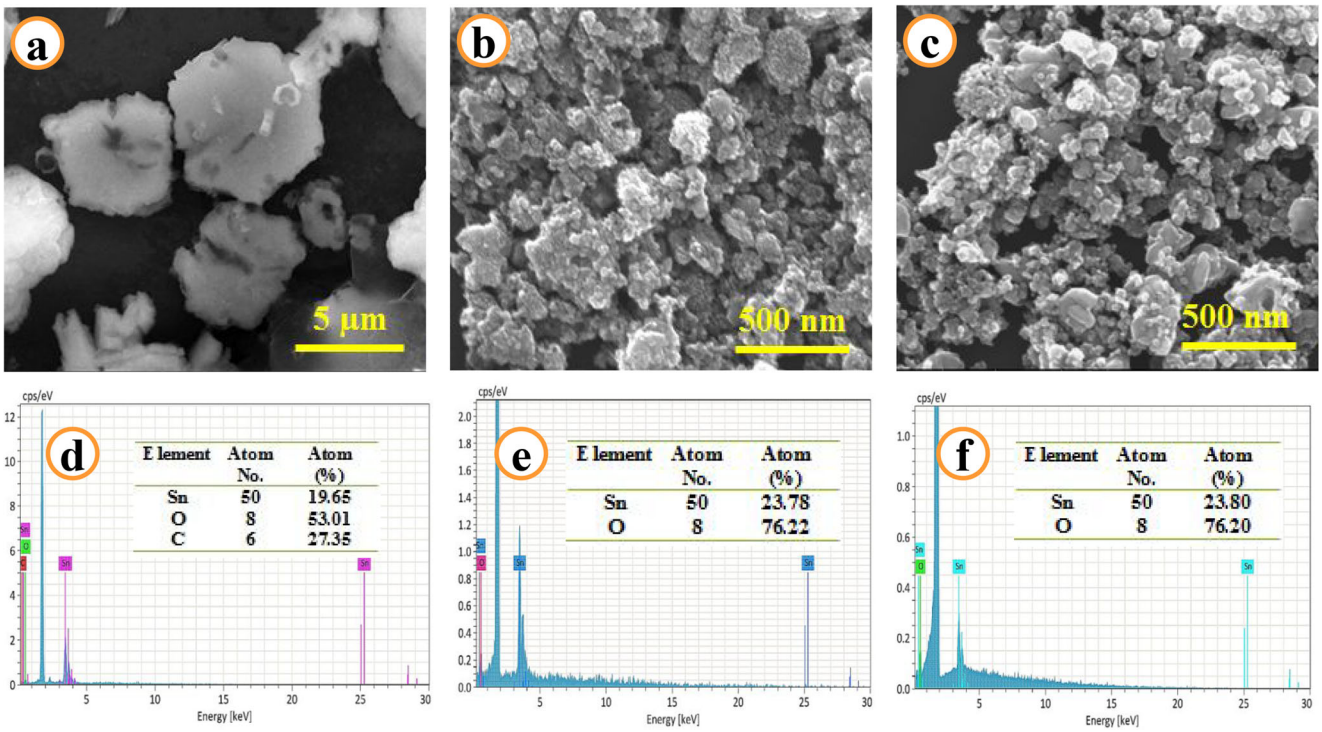

Fig. 5 The HR-SEM images of **a** tin oxyhydroxide-terephthalic acid composite, **b** SnO_2 (450 °C), and **c** SnO_2 (650 °C). **d**–**f** The EDS analysis of the tin oxyhydroxide-terephthalic acid composite, SnO_2 (450 °C), and SnO_2 (650 °C)

wt%), which is attributed to the decomposition of the acid group from terephthalic acid and hydroxide moiety of $Sn_6O_4(OH)_4$. The second minor weight loss noticed at 345.5 °C–440.5 °C (4.55 wt%) is accountable for the disintegration of the phenyl group. The SnO_2 obtained at 450 °C exhibits a weight loss from 380 to 500 °C, which attributes to the removal of the phenyl group [49]. It emphasizes the incomplete removal phenyl group during pyrolyzing at 450 °C. The SnO_2 obtained at 650 °C reveals almost no weight loss obtained. It highlights that the phenyl group has been completely eliminated.

Figure 5 depicts the HR-SEM images of the $Sn_6O_4(OH)_4$/TER composite and SnO_2 pyrolyzing at 450 °C and 650 °C. As can be seen from Fig. 5a, the synthesized $Sn_6O_4(OH)_4$/TER composite exhibits a fluffy flake-like structure and agglomerate which stacked upon each other. This flake does not easily separate as a monomer, due to interfacial tension between the small-sized flakes. The size of the particles was approximately 7 to 10 μm. These structures were assembled randomly. It can be evident from Fig. 5b and c the agglomeration of spherical SnO_2 nanospheres. The particles were randomly arranged and compactly packed. The elemental composition present in the synthesized material was examined with EDS spectra analysis as represented in Fig. 5d–f. The $Sn_6O_4(OH)_4$/TER composite was made up of carbon (27.35%), tin (19.65%), and oxygen (53.01). After pyrolyzing, the material showed the existence of tin and oxygen. The tin and oxygen content was almost identical composition irrespective of the pyrolyzing temperature.

Figure 6 a describes the HR-TEM image of the $Sn_6O_4(OH)_4$/TER composite, which exposes fluffy platelet-like morphology. It is evident from the figure that the terephthalic acid particles were dispersed on the $Sn_6O_4(OH)_4$ and prevent the agglomeration of the particles. Electron diffraction studies display both dots, and as well as ring patterns, confirming the crystalline nature of the $Sn_6O_4(OH)_4$ as seen in Fig. 6b. It can be observed from Fig. 6c that the produced SnO_2 shows the spherical shape particles with a size of 20–25 nm. The SAED pattern of the SnO_2 nanospheres is illustrated in Fig. 6d. The ring patterns were indexed to the (110), (101), and (211) planes of SnO_2 nanospheres. These planes' d-spacing values are in good agreement with results obtained from X-ray diffraction studies.

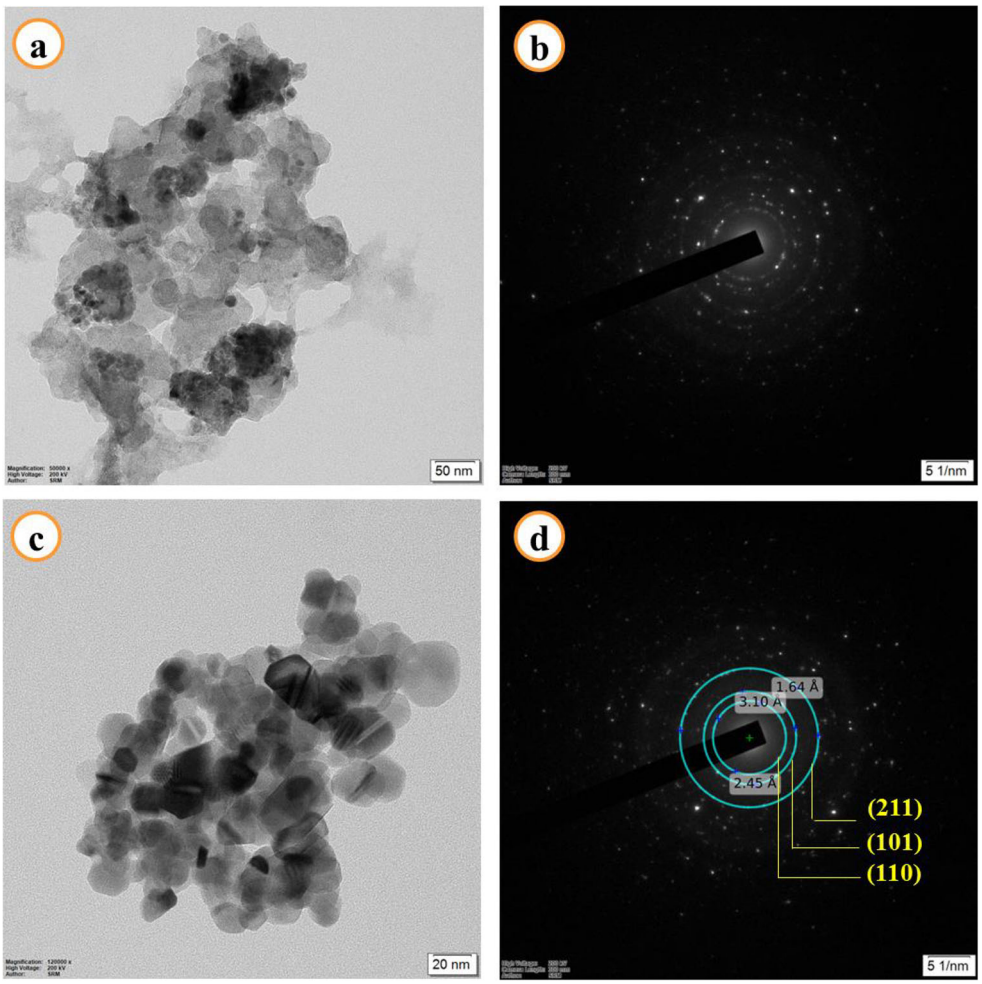

Fig. 6 The HR-TEM images of **a** tin oxyhydroxide-terephthalic acid composite and **c** SnO_2 (650 °C). **b**, **d** The SAED patterns of tin oxyhydroxide-terephthalic acid composite and SnO_2 (650 °C)

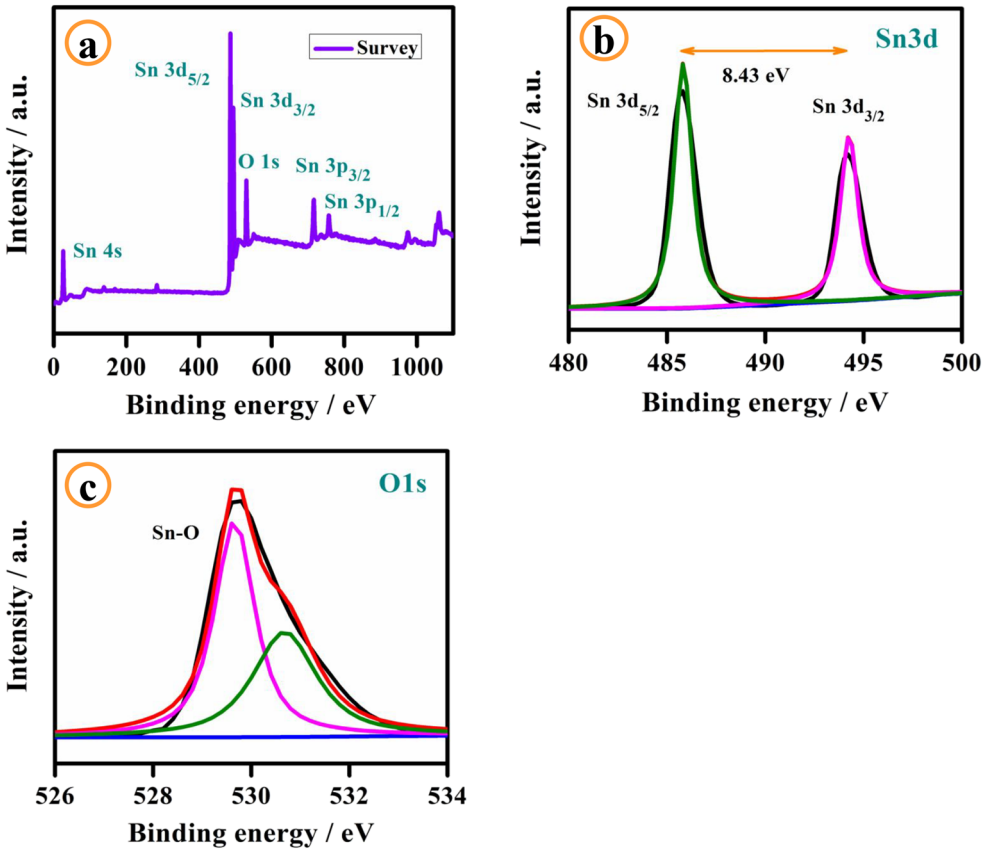

Fig. 7 The deconvoluted XP spectra of SnO_2 nanosphere acquired at 650 °C: **a** survey, **b** Sn 3d, and **c** O1s

Figure 7a depicts the overall survey X-ray photoelectron spectra of the SnO_2 nanospheres. It indicates that the existence of Sn, O, and other elements was not identified. Figure 7b reveals the fine spectrum of the Sn 3d region. The two strong peaks of Sn 3d are observed at 485.8 eV and 494.2 eV that corresponds to the Sn $3d_{5/2}$ and Sn $3d_{3/2}$. The binding energy value difference between Sn $3d_{5/2}$ and Sn $3d_{3/2}$ was 8.43 eV. It is confirmed from the results the Sn present in oxide form [50, 51]. Figure 7c illustrates the broad curve of the deconvoluted O 1s spectrum. The fitted two peaks centered at 529.6 eV and 530.6 eV were allotted to the Sn–O bond and chemisorbed oxygen, respectively [52, 53].

Figure 8a depicts the N_2 gas adsorption and desorption of the synthesized SnO_2 nanospheres. The isotherm reveals a type II isotherm with H3 hysteresis loops. The specific surface area calculated using the Brunauer–Emmer–Teller (BET) method and estimated to be 20.23 $m^2\ g^{-1}$. Figure 8b illustrates the Barrett–Joyner–Halenda (BJH) pore size distribution of the curve of the prepared SnO_2 nanospheres. It can be established from the pore distribution analysis that the synthesized SnO_2 material exists in mesoporous structure and exhibits the pore width and pore volume value of 8.84 nm and 0.075 $cm^3\ g^{-1}$, respectively. The low specific surface area may be attributed to the capacity fading during the charge–discharge process.

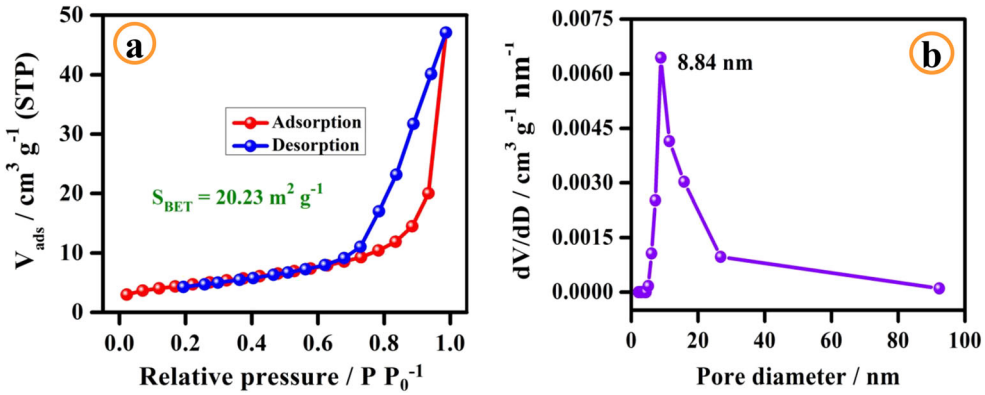

Fig. 8 **a** The plot of BET nitrogen adsorption–desorption isotherm and **b** BJH pore size distribution curve of the SnO_2 nanosphere

Electrochemical analysis

The preliminary information about the redox properties of the fabricated electrode is examined via cyclic voltammetric studies as exposed in Fig. 9a. In the first cathodic sweep, the reduction peaks that appeared at 1.04 V and 0.76 V are corresponding to the solid-electrolyte interphase formation (Eq. (1)) and transformation of SnO_2 to metallic Sn and Li_2O (Eq. (2)), respectively [1]. The cathodic peak at 0.15 V is associated with the Li_xSn alloy (Eq. (3)). The broad peak in the anodic region detected at 0.53 V is ascribed to the de-alloying of Li_xSn alloy. The oxidation peak at 1.25 V is an indication of the partial recovery of a few tin oxides [24, 26, 37]. Owing to the hysteresis in CV performance, the cathodic and anodic peaks are shifted into a negative direction and positive direction, respectively.

$$Li^+ + e^- + \text{electrolyte} \rightarrow \text{SEI films} \quad (1)$$

$$SnO_2 + 4Li^+ + 4e^- \rightarrow Sn + 2Li_2O \quad (2)$$

$$Sn + xLi^+ + xe^- \rightarrow Li_xSn\ (0 < x < 4.4) \quad (3)$$

Figure 9b represents discharge–charge profiles of the SnO_2 electrode in the potential limit of 0.01 to 2.0 V vs. Li/Li^+ in the 1st, 2nd, 3rd, 20th, and 50th cycles. The SnO_2 electrode provides first discharge and charge capacities of 1149 mAh g^{-1} and 704 mAh g^{-1}, respectively. The perceived discharge capacity of the second cycle is 720 mAh g^{-1}. The huge capacity loss during the second cycle is ascribed to the irretrievable construction of Li_2O, entangling of Li^+ ions in the lattice, solid electrolyte interphase film formation, and decomposition of solvents leading to the formation of inorganic products [4, 54]. It can be understood from the profile that the conquered plateau is reliable with the CV peaks.

The cyclic performance of the prepared SnO_2 electrode studied at 100 mA g^{-1} and the voltage limit between 0.01 and 2.0 V is shown in Fig. 9c. As expected, the fabricated SnO_2 electrode unveils high capacity retention, but the reversible capacity is about 52 mAh g^{-1} after 50 cycles. The coulombic efficiencies of the first four cycles were improved from 61 to 95% and then maintained at the level of 95%. The lower coulombic efficiency of the preliminary few cycles relates to the low surface area of the SnO_2 nanospheres, which influences the construction of profuse of SEI films and some Li_2O. After the fourth cycle, the coulombic efficiency of 95% sustained up to 50 cycles. It specifies the saturation of SEI film formation. It can be concluded from the above results that the prepared SnO_2 can be utilized as an anode to augment the electrochemical performance in rechargeable Li-ion battery. The energy storage character of synthesized SnO_2 nanospheres is compared with SnO_2 with different morphology, and SnO_2-based composite has been previously reported in the literature as described in Table 1.

Figure 9d demonstrates the high rate stability behavior of the SnO_2 nanospheres at different current rates. The initial discharge capacities of 1166, 528, 334, and 127mAh g^{-1} were provided by SnO_2 nanospheres at an applied current density of 100, 200, 400, and 600 mA g^{-1}, respectively. The reversible

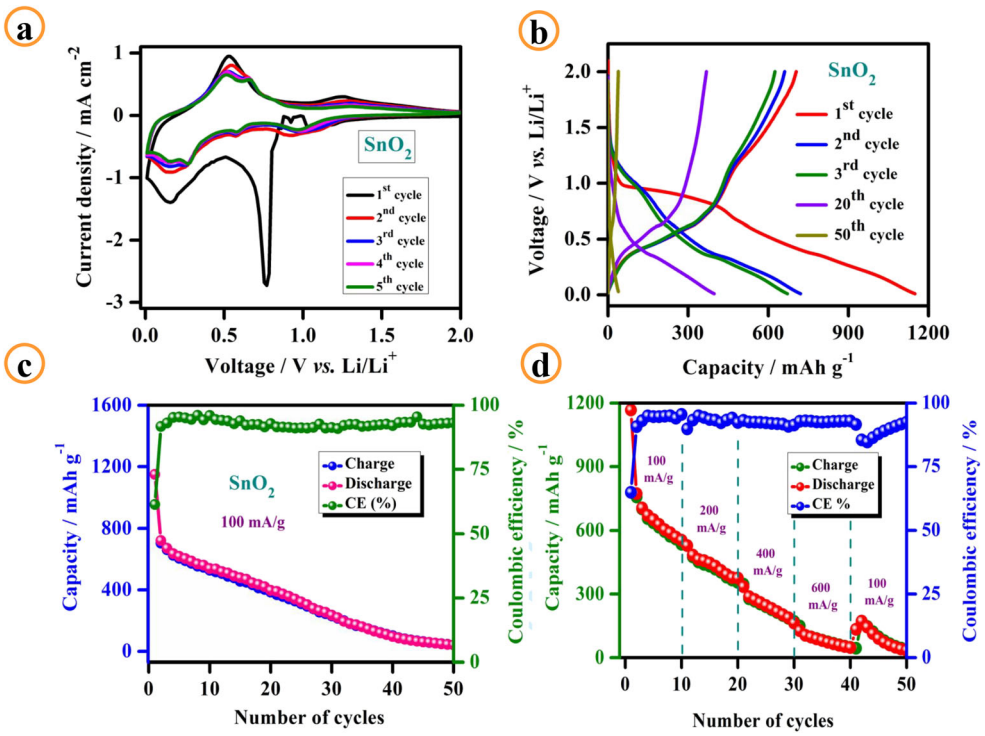

Fig. 9 The **a** cyclic voltammogram, **b** discharge–charge curves, **c** cycling stability studies, and **d** rate capability performance of the SnO_2 anode material calcined at 650 °C

Table 1 Comparison of the Li-ion energy storage performance of the present work with previously reported literature

Material	Preparation method	Morphology	Current (mA g^{-1})	Capacity (mAh g^{-1})	Ref.
SnO_2/MWCNT	Wet chemical	Sno_2 grain–coated MWCNTs	0.1 C	237/20th cycle	[55]
SnO_2	Microwave hydrothermal	Nanosheet	100	257.8/50th cycle	[56]
SnO_2	Microwave hydrothermal	Nanoparticles	100	272.6/50th cycle	[40]
SnO_2, SnO_2-C	Hydrothermal	Nanotube, nanotube	100	240/20th cycle 400/50th cycle	[57]
SnO_2	Anodic electrochemical deposition	Meso-scale tubes, microbowls	2 C	462/150th cycle 261/150th cycle	[58]
SnO_2, $SnTi_3O_7$ coupled SnO_2	Hydrothermal	Mesoporous spheres, $SnTi_3o_7$ nanowire–coupled SnO_2 nanoparticle	100	41/50th cycle 170/100th cycle	[59]
rGO/SnO_2	Silica template–assisted nanocasting process	Crumpled sheet–like plates	100	536/100th cycle	[60]
SnO_2	Co-precipitation	Nanosphere	100	52/50th cycle	This work

discharge capacities of 553, 375, 163, and 47 mAh g^{-1} were obtained at the end of 10, 20, 30, and 40 cycles, respectively. After 40 cycles, when the current density recovers to its initial rate of 100 mA g^{-1}, a discharge capacity of 172 mAh g^{-1} was acquired. After cycling at high current rate, the SnO_2 electrode undergoes large volume expansion and causes pulverization, which results in loss of cycling stability.

To understand the electrode¯electrolyte interface behavior of the electrode, electrochemical impedance spectroscopy is executed in a wide frequency range from 1 to 10 mHz. Figure 10a describes the Nyquist plot of the half-cell fabricated using SnO_2 electrode pre-cycling and post-cycling. The acquired EIS spectra exhibit a semi-circle in the high-frequency region and an inclined straight line in the low-frequency region. The resistance observed in the high-frequency region is assigned to solution resistance. The initial part of the semicircle is allocated to the SEI layer resistance of the fresh cell, and another part of the semi-circle relates to the charge transfer resistance. The slope line in the low-frequency region is allotted to lithium-ion diffusion [40]. It has quantitatively scrutinized with an equivalent circuit fitting for the fresh cell which is depicted in Fig. 10b. It entails uncompensated solution resistance (R_s = 6.27 Ω cm^2) and resistance (R_{SEI} = 51.89 Ω cm^2), and constant phase element (CPE_{SEI}) designates the SEI formation and charge transfer resistance (R_{ct} = 432.20 Ω cm^2), and constant phase element (CPE_d) specifies the double layer charging and discharging, and Z_w insist the Li-ion diffusion within the SnO_2 nanospheres. After cycling,

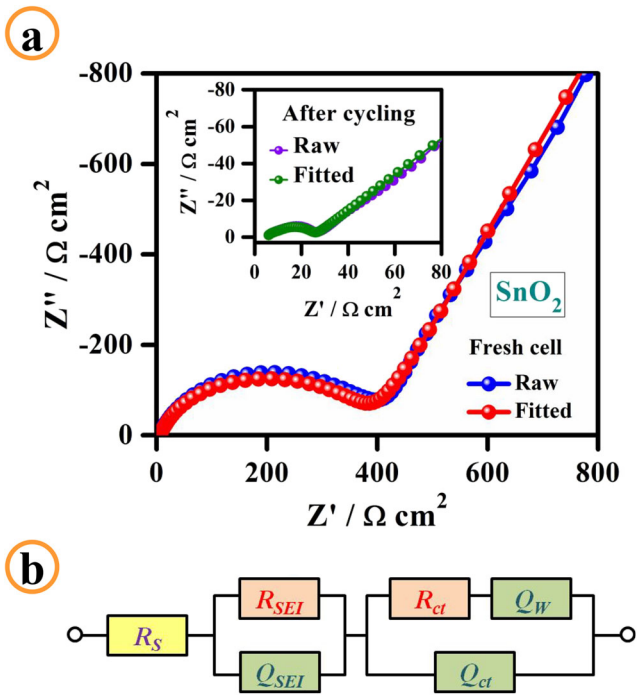

Fig. 10 The **a** electrochemical impedance spectra of the fabricated half-cell containing SnO_2 material pre-cycling and post-cycling (inset) and **b** fitted equivalent circuit model

the resistance of the SnO_2 electrode diminishes as shown in inset Fig. 10a. The impedance parameter values 5.96 Ω cm^2, 8.26 Ω cm^2, and 28.54 Ω cm^2 are associated with R_S, R_{SEI}, and R_{ct}, respectively. It can be concluded from the impedance results and charge transfer resistance values that the SnO_2 nanospheres simplify the Li-ion diffusion kinetics and enhance the interfacial reaction.

Conclusion

In summary, tin oxide–based nanosphere anode material was successfully synthesized via the co-precipitation method. HR-SEM shows $Sn_6O_4(OH)_4$-TER composite; SnO_2 exhibits a fluffy flake-like structure and nanospherical structure with an approximate size of 20 to 30 nm. Elemental composition analysis was specified of tin and oxygen present in an approximately 1:3 atomic ratio. The electrochemical properties of CV studies indicate that the SnO_2 undergoes conversion reaction (SnO_2 to Li_xSn). The charge–discharge curves exploit a high specific capacity of 1149 mAh g^{-1} at 100 mA g^{-1} in the first cycle. The coulombic efficiencies of the first four cycles were improved from 61 to 95% and then maintained at the level of 95% up to the end of cycles. The SnO_2 has deliberated as an efficient negative electrode for lithium-ion energy storage applications. It can be further developed via structural modification with transition elements and used for anode material in the Li-ion battery application.

Funding The study was financially supported by the Science and Engineering Research Board (SERB), a statutory body of the Department of Science & Technology (DST), Govt. of India (Project File No. ECR/2017/001156). The author S. Kumaraguru was provided fellowship by CSIR through the SRF-Direct scheme (File No. 09/1045(0037) 2K19 EMR-I). Also, this research was supported by Next Generation Engineering Researcher Program of National Research Foundation of Korea (NRF) funded by the Ministry of Science and ICT (No. 2017H1D8A2031138). Ministry of Human Resource Development RUSA- Phase 2.0 grant sanctioned vide Lt.No.F-24-51/2014 U Policy (TNMulti Gen), Dept. of Education, Govt. of India.

References

1. Li L, Liu X, Wang S, Zhao W (2014) Influence of surface structure on the capacity and irreversible capacity loss of Sn-based anodes for lithium ion batteries. ACS Sustain Chem Eng 2:1857–1863. https://doi.org/10.1021/sc500202m
2. Seenu P, Aravindan V, Lee YS (2017) Marine algae inspired pretreated SnO_2 nanorods bundle as negative electrode for Li-ion capacitor and battery: an approach beyond intercalation. Chem Eng J 324:26–34. https://doi.org/10.1016/j.cej.2017.05.003
3. Heubner C, Liebmann T, Voigt K, Weiser M, Matthey B, Junker N, Lammel C, Schneider M, Michaelis A (2018) Scalable fabrication of nanostructured tin oxide anodes for high-energy lithium-ion batteries. ACS Appl Mater Interfaces 10:27019–27029. https://doi.org/10.1021/acsami.8b07981
4. Winkler V, Kilibarda G, Schlabach S, Szabo DV, Hanemann T, Bruns M (2016) Surface analytical study regarding the solid electrolyte interphase composition of nanoparticulate SnO_2 anodes for Li-ion batteries. J Phys Chem C 120:24706–24714. https://doi.org/10.1021/acs.jpcc.6b06662
5. Bhaskar A, Deepa M, Rao TN (2014) Size-controlled SnO_2 hollow spheres via template free approach as anodes for lithium ion batteries. Nanoscale 6:10762–10771. https://doi.org/10.1039/C4NR02505A
6. Kim H, Cho J (2008) Superior lithium electroactive mesoporous Si@carbon core-shell nanowires for lithium battery anode material. Nano Lett 8:3688–3691. https://doi.org/10.1021/nl801853x
7. Ji X, Huang X, Liu J, Jiang J, Li X, Ding R, Hu Y, Wu F, Li Q (2010) Carbon-coated SnO_2 nanorod array for lithium battery anode material. Nanoscale Res Lett 5:649–653. https://doi.org/10.1007/s11671-010-9529-x
8. Wu R, Qian X, Yu F, Liu H, Zhou K, Wei J, Huang Y (2013) MOF-templated formation of porous CuO hollow octahedral for lithium-ion battery anode materials. J Mater Chem A 1:11126–11129. https://doi.org/10.1039/C3TA12621H
9. Su P, Liao S, Rong F, Wang F, Chen J, Li C, Yang Q (2014) Enhanced lithium storage capacity of Co_3O_4 hexagonal nanorings derived from Co-based metal organic frameworks. J Mater Chem A 2:17408–17414. https://doi.org/10.1039/C4TA02874K
10. Kong S, Dai R, Li H, Sun W, Wang Y (2015) Microwave hydrothermal synthesis of Ni-based metal-organic frameworks and their derived yolk-shell NiO for Li-ion storage and supported ammonia borane for hydrogen desorption. ACS Sustain Chem Eng 3:1830–1838. https://doi.org/10.1021/acssuschemeng.5b00556
11. Maiti S, Pramanik A, Dhawa T, Sreemany M, Mahanty S (2018) Bi-metal organic framework derived nickel manganese oxide spinel for lithium-ion battery anode. Mater Sci Eng B 229:27–36. https://doi.org/10.1016/j.mseb.2017.12.018
12. Cheong JY, Chang JH, Kim C, Lee J, Shim YS, Yoo SJ, Yuk JM, Kim ID (2019) Unveiling the origin of superior electrochemical performance in polycrystalline dense SnO_2 nanospheres as anodes for lithium-ion batteries. ACS Appl Energy Mater 2:2004–2012. https://doi.org/10.1021/acsaem.8b02103
13. Fu Q, Li R, Zhu X, Liang G, Luo L, Chen Y, Lin C, Zhao XS (2019) Design, synthesis and lithium-ion storage capability of $Al_{0.5}Nb_{24.5}O_{62}$. J Mater Chem A 7:19862–19871. https://doi.org/10.1039/C9TA04644E
14. Zhu X, Cao H, Li R, Fu Q, Liang G, Chen Y, Luo L, Lin C, Zhao XS (2019) Zinc niobate materials: crystal structures, energy-storage capabilities and working mechanism. J Mater Chem A 7:25537–25547. https://doi.org/10.1039/C9TA07818E
15. Fu Q, Zhu X, Li R, Liang G, Luo L, Chen Y, Ding Y, Lin C, Wang K, Zhao XS (2020) A low-strain $V_3Nb_{17}O_{50}$ anode compound for superior Li^+ storage. Energy Storage Mater 30:401–411. https://doi.org/10.1016/j.ensm.2020.05.012
16. Sotomayor ME, Torre-Gamarra CDL, Bucheli W, Amarilla JM, Varez A, Levenfeld B, Sanchez JY (2018) Additive-free $Li_4Ti_5O_{12}$ thick electrodes for Li-ion batteries with high electrochemical performance. J Mater Chem A 6:5952–5961. https://doi.org/10.1039/C7TA10683A
17. Wang H, Liang Q, Wang W, An Y, Li J, Guo L (2011) Preparation of flower-like SnO_2 nanostructures and their applications in gas sensing and lithium storage. Cryst Growth Des 11:2942–2947. https://doi.org/10.1021/cg2001255
18. Li L, Huang J, Wang T, Zhang H, Liu Y, Li J (2010) An excellent enzyme biosensor based on Sb-doped SnO_2 nanowires. Biosens Bioelectron 25:2436–2441. https://doi.org/10.1016/j.bios.2010.03.037
19. Wang G, Lu W, Li J, Choi J, Jeong Y, Choi SY, Park JB, Ryu MK, Lee K (2006) V-shaped tin oxide nanostructures featuring a broad

photocurrent signal: an effective visible-light-driven photocatalyst. Small 2:1436–1439. https://doi.org/10.1002/smll.200600216
20. Wang YF, Li JW, Hou YF, Yu XY, Su CY, Kuang DB (2010) Hierarchical tin oxide octahedral for highly efficient dye-sensitized solar cells. Chem Eur J 16:8620–8625. https://doi.org/10.1002/chem.201001333
21. Li Z, Tan Y, Huang X, Zhang W, Gao Y, Tang B (2016) Three-dimensionally ordered macroporous SnO_2 as anode materials for lithium ion batteries. Ceram Int 42:18887–18893. https://doi.org/10.1016/j.ceramint.2016.09.036
22. Min X, Sun B, Chen S, Fang M, Wu X, Liu Y, Abdelkader A, Huang Z, Liu T, Xi K, Vasant Kumar R (2019) A textile-based SnO_2 ultra-flexible electrode for lithium-ion batteries. Energy Storage Mater 16:597–606. https://doi.org/10.1016/j.ensm.2018.08.002
23. Kilibarda G, Szabo DV, Schlabach S, Winkler V, Bruns M, Hanemann T (2013) Investigation of the degradation of SnO_2 electrodes for use in Li-ion cells. J Power Sources 233:139–147. https://doi.org/10.1016/j.jpowsour.2013.01.099
24. Wei H, Xia Z, Xia D (2017) One step synthesis of uniform SnO_2 electrode by UV curing technology toward enhanced lithium-ion storage. ACS Appl Mater Interfaces 9:7169–7176. https://doi.org/10.1021/acsami.6b15820
25. Wei W, Song LX, Guo L (2015) SnO_2 hollow nanospheres assembled by single layer nanocrystals as anode material for high performance Li-ion batteries. Chin Chem Lett 26:124–128. https://doi.org/10.1016/j.cclet.2014.09.023
26. Yang T, Lu B (2014) Highly porous structure strategy to improve the SnO_2 electrode performance for lithium-ion batteries. Phys Chem Chem Phys 16:4115–4121. https://doi.org/10.1039/C3CP54144D
27. Park MS, Wang GX, Kang YM, Wexler D, Dou SX, Liu HK (2007) Preparation and electrochemical properties of SnO_2 nanowires for application in lithium-ion batteries. Angew Chem Int Ed 46:750–753. https://doi.org/10.1002/anie.200603309
28. Wang Z, Luan D, Boey FYC, Lou XW (2011) Fast formation of SnO_2 nanoboxes with enhanced lithium storage capability. J Am Chem Soc 133:4738–4741. https://doi.org/10.1021/ja2004329
29. Wang C, Zhou Y, Ge M, Xu X, Zhang Z, Jiang JZ (2010) Large-scale synthesis of SnO_2 nanosheets with high lithium storage capacity. J Am Chem Soc 132:46–47. https://doi.org/10.1021/ja909321d
30. Xu C, Sun J, Gao L (2012) Direct growth of monodisperse SnO_2 nanorods on graphene as high capacity anode materials for lithium batteries. J Mater Chem 22:975–979. https://doi.org/10.1039/C1JM14099J
31. Yang R, Gu Y, Li Y, Zheng J, Li X (2010) Self-assembled 3-D flower-shaped SnO_2 nanostructures with improved electrochemical performance for lithium storage. Acta Mater 58:866–874. https://doi.org/10.1016/j.actamat.2009.10.001
32. Wu P, Du N, Zhang H, Zhai C, Yang D (2011) Self-templating synthesis of SnO_2-carbon hybrid hollow sphere for superior reversible lithium ion storage. ACS Appl Mater Interfaces 3:1946–1952. https://doi.org/10.1021/am200168w
33. Gu F, Wang SF, Lu MK, Zhou GJ, Xu D, Yuan DR (2004) Photoluminescence properties of SnO_2 nanoparticles synthesized by sol-gel method. J Phys Chem B 108:8119–8123. https://doi.org/10.1021/jp036741e
34. Wang ZL (2003) Nanobelts, nanowires, and nanodiskettes of semiconducting oxides-from materials to nanodevices. Adv Mater 15:432–436. https://doi.org/10.1002/adma.200390100
35. Bruce PG, Scrosati B, Tarascon JM (2008) Nanomaterials for rechargeable lithium batteries. Angew Chem Int Ed 47:2930–2946. https://doi.org/10.1002/anie.200702505
36. Mukherjee R, Krishnan R, Lu TM, Koratkar N (2012) Nanostructured electrodes for high-power lithium ion batteries. Nano Energy 1:518–533. https://doi.org/10.1016/j.nanoen.2012.04.001
37. Hwang SM, Lim YG, Kim JG, Heo YU, Lim JH, Yamauchi Y, Park MS, Kim YJ, Dou SX, Kim JH (2014) A case study on fibrous porous SnO_2 anode for robust, high-capacity lithium-ion batteries. Nano Energy 10:53–62. https://doi.org/10.1016/j.nanoen.2014.08.020
38. Faramarzi MS, Abnavi A, Ghasemi S, Sanaee Z (2018) Nanoribbons of SnO_2 as a high performance Li-ion battery anode material. Mater Res Express 5:065040. https://doi.org/10.1088/2053-1591/aaca07
39. Zhao N, Deng L, Luo D, Mao Z, Zhan P (2019) Enhanced lithium storage performances of SnO_2 nanospheres induced by Sb dopants. Mater Res Express 6:045502. https://doi.org/10.1088/2053-1591/aafb42
40. Yin L, Chai S, Wang F, Huang J, Li J, Liu C, Kong X (2016) Ultrafine SnO_2 nanoparticles as a high performance anode material for lithium ion battery. Ceram Int 42:9433–9437. https://doi.org/10.1016/j.ceramint.2016.02.173
41. Wang B, Luo B, Li X, Zhi L (2012) The dimensionality of Sn anodes in Li-ion batteries. Mater Today 15:544–552. https://doi.org/10.1016/S1369-7021(13)70012-9
42. Ying H, Han WQ (2017) Metallic Sn-based anode materials: application in high-performance lithium-ion and sodium-ion batteries. Adv Sci 4:1700298. https://doi.org/10.1002/advs.201700298
43. Kumaraguru S, Kumar GG, Raghu S, Gnanamuthu RM (2018) Fabrication of ternary Ni-TiO_2-TiC composite coatings and their enhanced microhardness for metal finishing application. Appl Surf Sci 447:463–470. https://doi.org/10.1016/j.apsusc.2018.03.216
44. Kaprara E, Tziarou N, Kalaitzidou K, Simeonidis K, Balcells L, Pannunzio EV, Zouboulis A, Mitrakas M (2017) The use of Sn(II) oxy-hydroxide for the effective removal of Cr(VI) from water: optimization of synthesis parameters. Sci Total Environ 605-606:190–198. https://doi.org/10.1016/j.scitotenv.2017.06.199
45. Sledz M, Janczak J, Kubiak R (2001) New crystalline modification of terephthalic acid. J Mol Struct 595:77–82. https://doi.org/10.1016/S0022-2860(01)00493-8
46. Hu Z, Xu X, Wang X, Yu K, Liang C (2020) Ultrafine SnO_2 nanoparticles anchored in the porous corn straw carbon substrate for high-performance Li-ion batteries. J Alloys Compds 835:155446. https://doi.org/10.1016/j.jallcom.2020.155446
47. Kandasamy G, Surendran S, Chakrabarty A, Kale SN, Maity D (2016) Facile synthesis of novel hydrophilic and carboxyl-amine functionalized superparamagnetic iron oxide nanoparticles for biomedical applications. RSC Adv 6:99948–99959. https://doi.org/10.1039/C6RA18567C
48. Kitabayashi S, Koga N (2015) Thermal decomposition of tin(II) oxyhydroxide and subsequent oxidation in air: kinetic deconvolution of overlapping heterogeneous processes. J Phys Chem C 119:16188–16199. https://doi.org/10.1021/acs.jpcc.5b04975
49. Ma YH, Ge SW, Wang W, Sun BW (2015) Studies on the synthesis, structural characterization, Hirshfeld analysis and stability of apovincamine (API) and its co-crystal (terephthalic acid: Apovincamine = 1:2). J Mol Struct 1097:87–97. https://doi.org/10.1016/j.molstruc.2015.05.014
50. Chen XT, Wang KX, Zhai YB, Zhang HJ, Wu XY, Wei X, Chen JS (2014) A facile one-pot reduction method for the preparation of a SnO/SnO_2/GNS composite for high performance lithium ion batteries. Dalton Trans 43:3137–3143. https://doi.org/10.1039/C3DT52661E
51. Zhang J, Zhu Y, Cao C, Butt FK (2015) Microwave-assisted and large-scale synthesis of SnO_2/carbon-nanotube hybrids with high lithium storage capacity. RSC Adv 5:58568–58573. https://doi.org/10.1039/C5RA10314B

52. Wang L, Li J, Wang Y, Yu K, Tang X, Zhang Y, Wang S, Wei C (2016) Construction of 1D SnO_2-coated ZnO nanowire heterojunction for their improved n-butylamine sensing performances. Sci Rep 6:35079. https://doi.org/10.1038/srep35079
53. Kumaraguru S, Yesuraj J, Mohan S (2020) Reduced graphene oxide-wrapped micro-rod like Ni/Co organic-inorganic hybrid nanocomposite as an electrode material for high-performance supercapacitor. Compos Part B 185:107767. https://doi.org/10.1016/j.compositesb.2020.107767
54. Choi NS, Yao Y, Cui Y, Cho J (2011) One dimensional Si/Sn-based nanowires and nanotubes for lithium-ion energy storage materials. J Mater Chem 21:9825–9840. https://doi.org/10.1039/C0JM03842C
55. Wang Z, Chen G, Xia D (2008) Coating of multi-walled carbon nanotube with SnO_2 films of controlled thickness and its application for Li-ion battery. J Power Sources 184:432–436. https://doi.org/10.1016/j.jpowsour.2008.03.028
56. Narasimulu D, Vinoth S, Srinadhu ES, Satyanarayana N (2018) Surfactant-free microwave hydrothermal synthesis of SnO_2 nanosheets as an anode material for lithium battery application. Ceram Int 44:201–207. https://doi.org/10.1016/j.ceramint.2017.09.159
57. Wu P, Du N, Zhang H, Yu J, Qi Y, Yang D (2011) Carbon-coated SnO_2 nanotubes: template-engaged synthesis and their application in lithium-ion batteries. Nanoscale 3:746–750. https://doi.org/10.1039/C0NR00716A
58. Chou SL, Wang JZ, Liu HK, Dou SX (2009) SnO_2 meso-scale tubes: one-step, room temperature electrodeposition synthesis and kinetic investigation for lithium storage. Electrochem Commun 11:242–246. https://doi.org/10.1016/j.elecom.2008.11.017
59. Wang H, Wang M, Li B, Yang X, Safarova K, Zboril R, Rogach AL, Leung HKH (2014) Hydrothermal synthesis and electrochemical properties of tin titanate nanowires coupled with SnO_2 nanoparticles for Li-ion batteries. CrystEngComm 16:7529–7535. https://doi.org/10.1039/c4ce00682h
60. Zhou D, Song WL, Li X, Fan LZ (2016) Hierarchical porous reduced graphene oxide/ SnO_2 networks as highly stable anodes for lithium-ion batteries. Electrochim Acta 207:9–15. https://doi.org/10.1016/j.electacta.2016.04.151